Atomic-Scale Quantification of Grain Boundary Segregation in Nanocrystalline Material

M. Herbig,[1,*] D. Raabe,[1,†] Y. J. Li,[1] P. Choi,[1] S. Zaefferer,[1] and S. Goto[1,2]
[1]*Max-Planck-Institut für Eisenforschung, Max-Planck-Strasse 1, 40237 Düsseldorf, Germany*
[2]*Department of Materials Science and Engineering, Faculty of Engineering and Resource Science,*
Akita University, Tegata Gakuencho, Akita 010-8502, Japan

(Received 25 October 2013; published 27 March 2014)

Grain boundary segregation leads to nanoscale chemical variations that can alter a material's performance by orders of magnitude (e.g., embrittlement). To understand this phenomenon, a large number of grain boundaries must be characterized in terms of both their five crystallographic interface parameters and their atomic-scale chemical composition. We demonstrate how this can be achieved using an approach that combines the accuracy of structural characterization in transmission electron microscopy with the 3D chemical sensitivity of atom probe tomography. We find a linear trend between carbon segregation and the misorientation angle ω for low-angle grain boundaries in ferrite, which indicates that ω is the most influential crystallographic parameter in this regime. However, there are significant deviations from this linear trend indicating an additional strong influence of other crystallographic parameters (grain boundary plane, rotation axis). For high-angle grain boundaries, no general trend between carbon excess and ω is observed; i.e., the grain boundary plane and rotation axis have an even higher influence on the segregation behavior in this regime. Slight deviations from special grain boundary configurations are shown to lead to unexpectedly high levels of segregation.

DOI: 10.1103/PhysRevLett.112.126103 PACS numbers: 68.35.Dv, 68.35.bd, 68.37.Lp, 68.37.Vj

Most materials are polycrystalline; i.e., they consist of volumes of regularly arranged atoms (grains) and interfaces where differently oriented grains meet [grain boundaries (GBs)]. The lattice mismatch at GBs causes local structural disorder and an excess energy associated with the interface. The system can reduce its free energy by diffusion (here by equilibrium segregation) of solutes to the GB according to the Gibbs adsorption isotherm [1–3]. This change in chemistry happens only within some tens of nanometers around the GB; however, the local compositional changes can be drastic: some elements can be enriched by a factor of 10^6 as compared to their bulk solubility [4].

These local chemical changes affect the material's macroscopic behavior profoundly [5,6], as GBs in polycrystalline materials form a 3D interconnected network. For instance, changes in grain cohesion and electrochemical properties due to solute segregation can alter fracture toughness and corrosion of metallic alloys by orders of magnitude (e.g., hydrogen embrittlement [7] and stress corrosion cracking [8]). The addition of only 0.6 wt % phosphorous to iron reduces fracture toughness at room temperature by a factor of ~50 [9]. Interfacial chemistry also affects GB energy and mobility, and through this grain coarsening as well as the stability of nanostructures [10,11]. Local solute decoration can lead to the nucleation of second phases, formation of complexions [12], or selective melting of GBs [13]. Additionally, semiconductors are affected by GB segregation due to band structure changes that alter the recombination activity of charge carriers [14].

Despite its enormous importance, GB segregation is far from being understood. The reason for this is the immense experimental challenge associated with its quantitative characterization: The description of a GB requires the measurement of five crystallographic parameters, each of which influences segregation. Three independent parameters quantify the misorientation between neighboring grains, i.e., a normalized rotation axis and an angle about it. Two more parameters describe the GB plane normal. Atomistically, there are even three more parameters describing atomic relaxation, but as these cannot be considered to be independent [15], they are neglected here. This leaves us with a 5D parameter space, including steep variations, to be screened for correlations between crystallography and segregation. Hence, a large number of grain boundaries must be quantified. Since the Gibbs adsorption is an atomic-scale phenomenon, an analytical tool is needed that is precise enough to capture even minor traces of segregation at grain boundaries irrespective of elemental mass and with near-atomic spatial resolution. Moreover, joint chemical and crystallographic characterization must be performed on the same sample at the same location.

GB segregation is commonly analyzed by Auger electron spectroscopy, secondary ion mass spectroscopy, analytical electron microscopy, field ion microscopy, or atom probe tomography (APT) [16]. These techniques provide only average values that were taken on segregation-embrittled systems, or they lack crystallographic information, chemical and/or spatial resolution, or statistics. To solve this fundamental problem, we jointly employ two complementary characterization methods with excellent analytical and structural precision: One is atom probe tomography, where individual surface atoms are field evaporated from a needle-shaped sample in a strong electric field and accelerated towards a position-sensitive detector. APT, a combination of time-of-flight mass spectrometry and ion projection microscopy provides 3D compositional information with equal detection sensitivity (a few ppm) for all elements at near-atomic resolution [17]. However, its spatial resolution depends on the experimental conditions and only in special cases provides information on GB crystallography [18]. The second method is transmission electron microscopy (TEM), which enables crystallographic characterization down to the subnanometer scale; however, accurate quantification of local chemical composition in 3D is only possible in special cases. Consequently, the correlative application of these complementary techniques to identical sample positions is an ideal method for GB characterization.

Here we show how this aim can be reached with a setup for optimized TEM measurement conditions conducted on atom probe tips [Figs. 1(a)–1(c)]. As described by Felfer *et al.* [19], the samples were extracted from the surface of the bulk, deposited on a halved TEM grid, sharpened by focus ion beam (FIB) milling, investigated by TEM, and subsequently analyzed by APT. Up to four samples were mounted on a single grid, enabling time-efficient batch sample fabrication and characterization. Our specific approach involves mounting the grids in a modified high-angle single-tilt TEM retainer, which enables the exact control of the sample orientation in all instruments by the use of self-designed adapters. This allows shaping the samples by FIB milling in such a way that their axis of rotational symmetry is parallel to the tilt axis in TEM. Using the three translational degrees of freedom in TEM, the sample and tilt axes are brought into coincidence, which is what ensures constant focus conditions over the entire sample volume during the TEM single-tilt operation. Using this setup, nanocrystalline atom probe tips containing multiple GBs per sample can be characterized by TEM, allowing for drastically increased throughput as compared to former setups that were limited to one grain boundary per sample [20].

We demonstrate this technique using heavily cold-drawn pearlitic steel with the composition Fe–4.40C–0.30Mn–0.39Si–0.21Cr (at. %), slightly annealed for 2 min at 400° C to generate a microstructure of columnar grains with a diameter of ~30 nm [21]. For the interpretation of our experimental results, we assume the carbon distribution in this material to be at diffusive equilibrium. A TEM characterization of APT specimens was performed along the direction of the columnar grains to minimize the grain overlap. The grain boundary orientations were extracted from bright-field scanning TEM (STEM) images taken at 200 kV in a JEOL JEM-2200FS with a spot size of 1.5 nm and 16 μs dwell time [Fig. 1(d)]. Using this short dwell time, beam damage, as reported by Özkaya *et al.* [22] during STEM electron energy loss spectrometry (EELS) characterization of phosphorous GB segregation in iron, was not observed. The grain orientations were measured by nanobeam diffraction (NBD) [23] in parts manually, point by point in STEM spot mode followed by indexing of the diffraction patterns using TOCA software [24]. Alternatively, nanobeam diffraction was performed in scanning mode using the commercial package ASTAR [25,26] at 0.5 nm spot size and 2 nm step size. Approximately 150 × 75 measurement points were collected per sample [Fig. 1(e)] corresponding to about a 15 min measurement time. In addition to a high degree of automation, the scanning NBD approach has the strong advantage that the diffraction patterns for each measurement point can be recorded. This enables offline data analyses after the destructive atom probe experiment. APT measurements were

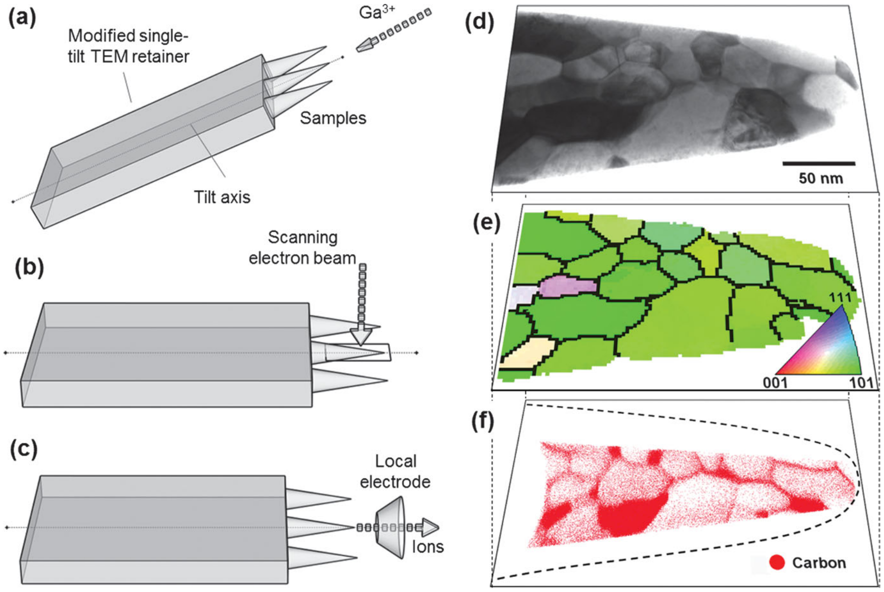

FIG. 1 (color). Experimental setup and output data. After a sample fabrication by focused ion beam milling (a), transmission electron microscopy (b) is used to measure grain boundary orientations in STEM mode (d) and grain orientations by scanning nanobeam diffraction (e). Finally, atom probe tomography (c) is used to reconstruct a 3D atom map (f).

conducted with a local electrode atom probe (LEAP 3000X HR, Cameca Instruments) in voltage mode at 70 K, with a pulse fraction of 15%, a pulse repetition rate of 200 kHz, and a detection rate of 0.01 atoms per pulse. The parameters for the reconstruction of the 3D atom map [Fig. 1(f)] were optimized using the STEM images as templates, thereby minimizing distortions of the reconstructed volume.

Figures 2 and 3 illustrate the degree of accuracy that can be achieved with the present approach. The overlay between the 2D projection of the 3D atom map and the STEM image shows excellent agreement. GBs and even individual dislocation lines within low-angle GBs (Fig. 3) are clearly visible in the STEM image. Most of the GBs were parallel to the electron beam in TEM, and, hence, they are visible as single lines in the STEM images [single yellow arrow in the center of Fig. 3(d)]. In this case, their orientation could be determined directly from the normal to this line. In the case of slightly inclined boundaries, two lines are visible, one for each intersection of the boundary with the upper and lower surfaces of the sample [pairs of yellow arrows in Fig. 3(d)]. Here, first the local thickness of the sample was estimated from the local width of the sample, as observed in the STEM images, assuming the sample to be a conical object. Then, the distance between the lines was related to two possible inclination angles of the boundary. The correct inclination angle was identified based on the 3D atom maps. The Gibbs interfacial excess values of carbon in atoms/nm^2 were determined from cumulative plots of carbon atoms against all elements (so-called ladder diagrams, for details, see Ref. [27]) along the rectangular regions of interest, which were positioned perpendicularly across the GBs in the 3D atom maps.

In total, 121 GBs were measured on seven samples in only six days of experimental time; this established a very efficient high throughput approach providing access to all crucial parameters and enabled us for the first time to study systematically the physics and chemistry of GBs as a function of five crystallographic parameters. Figure 4(b) shows the carbon excess plotted over the misorientation angle ω, which is often considered the most influential crystallographic parameter with respect to the physical properties of grain boundaries. A clear trend of increasing carbon excess with increasing misorientation angle is visible up to about 14°. This is the regime of low-angle grain boundaries (LAGBs), which consist of dislocations whose density increases with the misorientation angle. As most carbon atoms are absorbed by the dislocation cores [28], which do not overlap also for higher misorientation angles of up to 15°, we used a linear expression to fit the grain boundary excess Γ in this regime: $\Gamma = K\omega$. The fitting parameter K was determined as 0.40 ± 0.04 atoms$(°)^{-1}$ nm^{-2}. Above $\omega \approx 14°$, the misorientation is too high to be structurally accommodated by dislocations, and we enter the regime of high-angle grain boundaries (HAGBs). Here the variation of carbon excess for a given misorientation angle is significantly higher than in the regime of LAGBs; at around 60°, the carbon excess ranges between 0 and 15 excess carbon atoms/nm^2 [Fig. 4(b)].

The accuracy of Fig. 4(b) is mainly determined by two factors: First, by the angular resolution of the nanobeam diffraction, typically ≤1° [25], and second, by the error due to manual peak fitting of the ladder diagrams, which was estimated by determining the upper and lower bounds to not exceed ±1 atoms/nm^2 (gray error bars). As these errors are small compared to the measured values, the spread of the data points in Fig. 4(b) can be considered a reliable signal. We, therefore, attribute the large distribution of concentrations for the same misorientation angle to the fact that the diagram takes only one out of five crystallographic parameters into account, i.e., that it is a projection of the carbon excess distribution in 5D space. For the regime of LAGBs, this means that the ratio

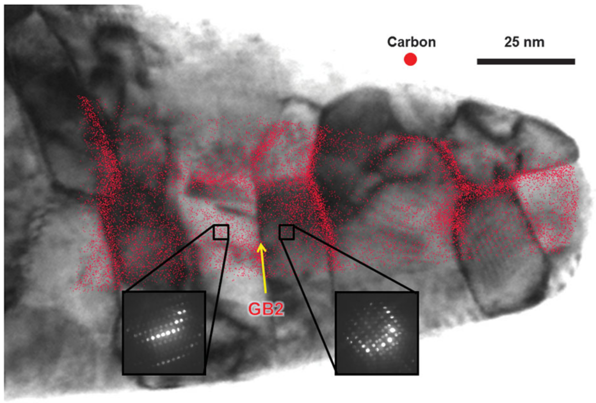

FIG. 2 (color). Overlay of projected 3D atom map and bright-field STEM micrograph of a pearlitic steel atom probe specimen. Grain orientations are determined by nanobeam diffraction in the TEM. GB2, a $\Sigma3$ coherent twin, shows significantly lower carbon segregation than the average grain boundary [see, also, Fig. 4(b)].

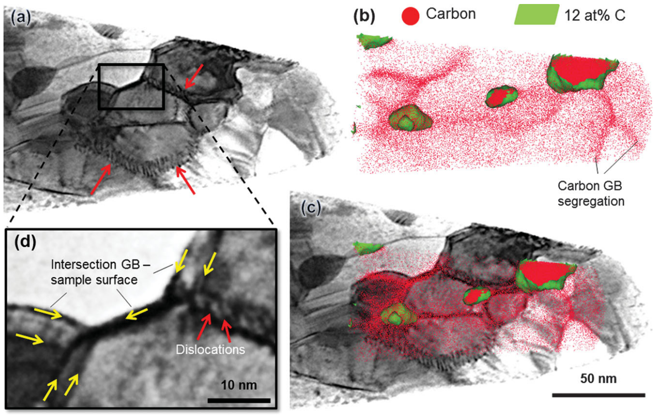

FIG. 3 (color). (a) Bright-field STEM micrograph of a pearlitic steel atom probe specimen. Red arrows mark dislocation lines along low-angle grain boundaries. (b) Projection of 3D atom map. Red dots mark carbon atoms. Carbides are highlighted by green envelopes (12 at. % isoconcentration surfaces). (c) Overlay of (a) and (b). (d) Magnification of (a). Yellow arrows mark the intersections of grain boundaries with upper/lower sample surface.

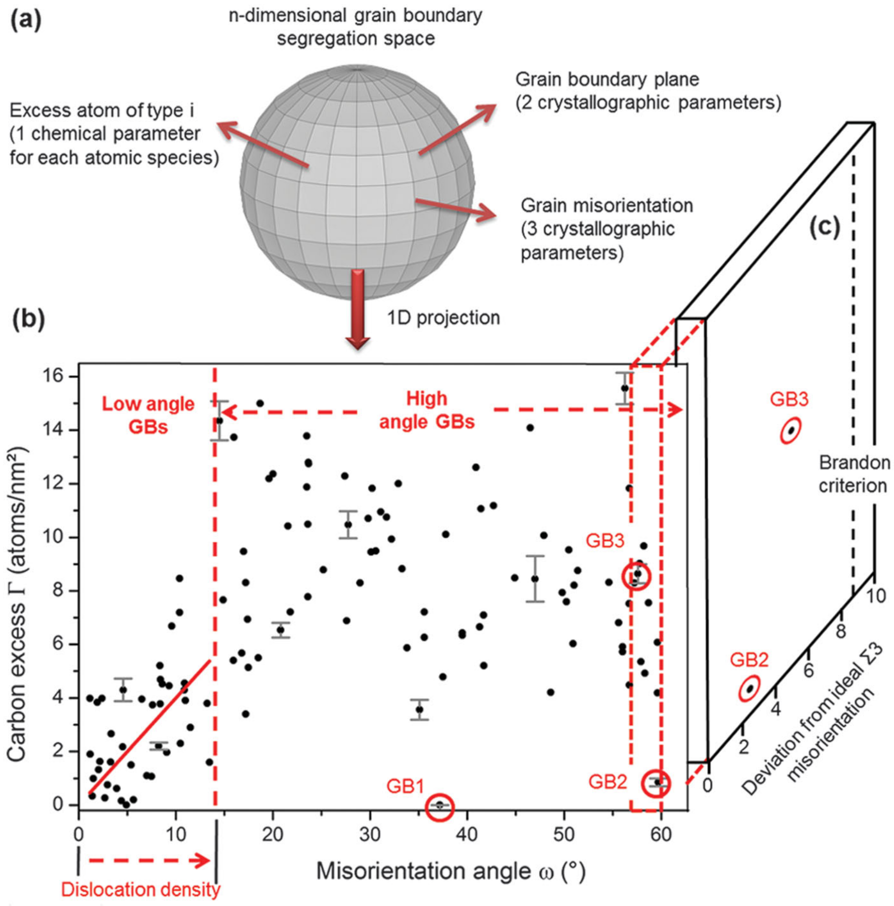

FIG. 4 (color). Plot of carbon excess in grain boundary space. For reasons of visualization the *n*-dimensional grain boundary segregation space (a) is projected into a 1D plot showing carbon excess, Γ, over misorientation angle, ω, for 121 grain boundaries in ferrite (b). Error bars estimated by determining the upper and lower bounds for manual peak fitting of Γ are marked in gray. A linear fit corresponding to the increase in dislocation density was performed for the low-angle regime (red line). The strong spread of data points for $\omega > 14°$ is attributed to the large influence of the four crystallographic parameters in the high-angle regime that are not taken into account in this diagram. GB1-3 are the Σ5, Σ3, and Σ3 boundaries, respectively. The difference in carbon segregation between GB2 and 3 can be understood with the help of (c). The high deviation from the ideal Σ3 misorientation of GB3 means the presence of misfit dislocations which are responsible for the measured carbon segregation.

of screw to edge dislocations (which absorb different amounts of carbon) in the boundary as well as the twist or tilt character (for a given misorientation angle, a twist GB contains twice as many dislocations than a tilt GB) are not taken into account. The fact that there is a stronger spread of carbon segregation in the high-angle regime as compared to the low one indicates that taking all crystallographic parameters into account is even more essential for the high-angle regime.

The GBs 1–3 in Fig. 4(b) mark special boundaries. GB1 is a Σ5 boundary; GB2 and 3 can be both identified as Σ3 coherent twins (60°[111]{112}). Both boundary types are known for their high coherence and their energy that is much lower than the energy of a typical HAGB, so only very little or no segregation would be expected [29]. This is, indeed, the case for GBs 1 and 2 (see GB2 in Fig. 2) but surprisingly not for GB3. This distinct difference can be explained by the angular deviation from the ideal Σ5 or Σ3 misorientation (not taking the GB plane into account), which is 0.7°, 2.3°, and 4.8° for GBs 1–3, respectively. While GBs 1 and 2 are within or close to the range of angular resolution and could be ideally coherent GBs, GB3 is clearly out of this range—a deviation that is accommodated by misfit dislocations. Most probably GB3 formed during cold drawing and rotated away from its ideal configuration by the agglomeration of secondary GB dislocations. These dislocations attract carbon what explains part of the carbon segregation measured at this boundary. Assuming the highest possible angular measurement error of 1° per grain, the dislocation density of GB3 should not exceed the one of a LAGB with a 6.8° misorientation angle. With $8.6 \pm 0.4\ \mathrm{nm}^{-2}$, the amount of segregation at GB3 is surprisingly higher than the highest levels measured for the corresponding LAGBs ($5.2\ \mathrm{nm}^{-2}$). This discrepancy can only be explained by a strong influence of the GB plane orientation. The angular deviation between the grain boundary plane and the closest {112} plane of each grain is higher in case of GB3 (2.8° and 4.0°) than in the case of GB2 (1.5° and 1.7°). A deviation from the ideal symmetry plane for a Σ3 boundary is accommodated by faceting [30,31] which is related to the formation of structural elements that include partial dislocations [32] or elastic strain [33]. Both sorts of defects (partial dislocations and elastic strain fields) may lead to an increase of carbon segregation at the boundary. The higher deviation from the ideal symmetry plane of GB3 could explain the additional carbon segregation measured here. The comparison of GB2 and 3 demonstrates the necessity of considering all crystallographic parameters when quantifying segregation.

The method described here is generally applicable to any nanocrystalline material with columnar grains that can be measured by APT. In addition, equiaxed nanocrystalline materials could be characterized by performing tomographic TEM orientation mapping [34]. In principle, the analysis described here could also be done by TEM only, using TEM imaging to characterize the boundary plane and STEM EELS to determine the carbon content. EELS is a powerful tool that gives a wealth of information on elemental concentrations, bonding and valence state, nearest-neighbor atomic structure, free-electron density, local thickness, etc. [35]. However, all of the information is convoluted in a single spectrum, and this is what makes the quantification of absolute values challenging. A quantitative analysis of carbon by EELS is particularly difficult, as hydrocarbon contamination forming in the electron beam continuously changes the EELS spectrum. In contrast to EELS, APT is mainly sensitive to information on elemental distribution. The elements can be directly identified by their mass-to-charge ratio, and in most cases, the overlapping peaks can be easily deconvoluted by considering the natural isotope abundances. Overall, APT is a robust, fast, and reliable technique to quantify local chemical compositions and, therefore, was used jointly with TEM for this study.

The high throughput of the method described here enables, for the first time, a precise as well as statistically robust analysis of the grain boundary segregation space. The experimental setup developed for this approach allows for the handling and characterization of atom probe samples as per normal TEM specimens. This configuration, thereby, opens the door to a large variety of correlative chemical and crystallographic investigations at the nanometer scale.

The authors are grateful to the German Research Foundation (Deutsche Forschungsgemeinschaft, DFG) that funded the project through SFB 761 “steels ab initio.” The authors acknowledge Dr. H. Yarita from Suzuki Metal Industry Co., LTD., Japan, for providing the cold-drawn specimens and Dr. P. Konijnenberg for support with the misindexing calculation.

---

[*] Corresponding author.
m.herbig@mpie.de
[†] Corresponding author.
d.raabe@mpie.de

[1] I. Langmuir, J. Am. Chem. Soc. **40**, 1361 (1918).
[2] J. W. Gibbs, *The Collected Works of J. Willard Gibbs* (Yale University Press, New Haven, CT, 1948), Vol. 1.
[3] D. McLean, *Grain Boundaries in Metals* (Oxford University Press, London, 1957).
[4] M. P. Seah and E. D. Hondros, Proc. R. Soc. A **335**, 191 (1973).
[5] P. Lejcek and S. Hofmann, Crit. Rev. Solid State Mater. Sci. **20**, 1 (1995).
[6] M. J. Duarte *et al.*, Science **341**, 372 (2013).
[7] H. C. Rogers Science **159**, 1057 (1968).
[8] A. King, G. Johnson, D. Engelberg, W. Ludwig, and J. Marrow, Science **321**, 382 (2008).
[9] W. A. Spitzig, Metall. Trans. **3**, 1183 (1972).
[10] R. Kirchheim, Acta Mater. **50**, 413 (2002).
[11] T. Chookajorn, H. A. Murdoch, and C. A. Schuh, Science **337**, 951 (2012).
[12] M. P. Harmer, Science **332**, 182 (2011).
[13] J. K. Heuer, P. R. Okamoto, N. Q. Lam, and J. F. Stubbins, Appl. Phys. Lett. **76**, 3403 (2000).
[14] J. Y. W. Seto, J. Appl. Phys. **46**, 5247 (1975).
[15] D. Wolf, *Atomic-Level Geometry of Crystalline Interfaces* (Chapman & Hall, London, 1992), pp. 1–57.
[16] P. Lejcek, *Grain Boundary Segregation in Metals* (Springer–Verlag, Berlin, 2010).
[17] T. F. Kelly and D. J. Larson, Annu. Rev. Mater. Res. **42**, 1 (2012).
[18] P. V. Liddicoat, X. Z. Liao, Y. H. Zhao, Y. T. Zhu, M. Y. Murashkin, E. J. Lavernia, R. Z. Valiev, and S. P. Ringer, Nat. Commun. **1**, 63 (2010).
[19] P. J. Felfer, T. Alam, S. P. Ringer, and J. M. Cairney, Microsc. Res. Tech. **75**, 484 (2012).
[20] B. W. Krakauer, J. G. Hu, S. M. Kuo, R. L. Mallick, A. Seki, D. N. Seidman, J. P. Baker, and R. J. Loyd, Rev. Sci. Instrum. **61**, 3390 (1990).
[21] Y. J. Li, P. Choi, S. Goto, C. Borchers, D. Raabe, and R. Kirchheim, Acta Mater. **60**, 4005 (2012).
[22] D. Ozkaya, J. Yuan, L. M. Brown, and P. E. J. Flewitt, J. Microsc. **180**, 300 (1995).
[23] S. Zaefferer, Adv. Imaging Electron Phys. **125**, 355 (2002).
[24] S. Zaefferer, J. Appl. Crystallogr. **33**, 10 (2000).
[25] P. Moeck, S. Rouvimov, E. F. Rauch, M. Véron, H. Kirmse, I. Häusler, W. Neumann, D. Bultreys, Y. Maniette, and S. Nicolopoulos, Cryst. Res. Technol. **46**, 589 (2011).
[26] E. F. Rauch, J. Portillo, S. Nicolopoulos, D. Bultreys, S. Rouvimov, and P. Moeck, Z. Kristallogr. **225**, 103 (2010).
[27] B. W. Krakauer and D. N. Seidman, Phys. Rev. B **48**, 6724 (1993).
[28] E. Clouet, S. Garruchet, H. Nguyen, M. Perez, and C. S. Becquart, Acta Mater. **56**, 3450 (2008).
[29] N. Gao, C. C. Fu, A. Samaras, R. Schaublin, M. Victoria, and W. Hoffelner, J. Nucl. Mater. **385**, 262 (2009).
[30] A. Brokman, P. D. Bristowe, and R. W. Balluffi, Scr. Metall. **15**, 201 (1981).
[31] B. B. Straumal, S. A. Polyakov, E. Bischoff, W. Gust, and E. J. Mittemeijer, Interface Sci. **9**, 287 (2001).
[32] M. A. Tschopp and D. L. McDowell, J. Mater. Sci. **42**, 7806 (2007).
[33] K. L. Merkle and D. Wolf, Philos. Mag. A **65**, 513 (1992).
[34] H. H. Liu, S. Schmidt, H. F. Poulsen, A. Godfrey, Z. Q. Liu, J. A. Sharon, and X. Huang, Science **332**, 833 (2011).
[35] D. B. Williams and C. B. Carter, *Transmission Electron Microscopy, Part 4: Spectrometry* (Springer, New York, 2009), 2nd ed.